Assembly and characterization of colloid-based antireflective coatings on multicrystalline silicon solar cells

Brian G. Prevo,† Emily W. Hon and Orlin D. Velev*

Received 4th September 2006, Accepted 10th November 2006
First published as an Advance Article on the web 27th November 2006
DOI: 10.1039/b612734g

Evaporation from a moving meniscus was used for controlled convective assembly of colloidal silica nanoparticles into antireflective coatings (ARCs) onto the rough uneven surfaces of polycrystalline silicon solar cells. The nanocoatings reduced the reflectance of the solar cells by approximately 10% across the near UV to near IR spectral range, which provided a 17% increase in the output power of the devices (which translated to a 10% relative increase in the efficiency). Microstructural analysis *via* SEM showed that while the surface coverage was uniform over long ranges, the thickness of the particle coatings varied locally due to the rough, undulating substrate surface. The UV/vis reflectance data of the silica coated solar cells could be modelled with the Fresnel reflectance relation by assuming a distributed range of thicknesses for the coatings, in good agreement with the microstructural data. We show that particulate films deposited on rough surfaces can function as ARCs even though they do not attain 0% reflectance. These silica particle-based coatings can be further modified by attachment of monolayers of fluorosilanes, which may make them superhydrophobic and/or self-cleaning.

1 Introduction

Photovoltaic (PV) devices such as solar cells (SCs) generate electrical current when photons with sufficient energy penetrate the semiconductor and excite electrons into the conduction band. One of the key problems in the fabrication of photovoltaic devices is the low energy conversion efficiency, which can be improved by advanced materials chemistry and refinements in semiconductor microfabrication.[1–7] A common problem outside of the PV material, however, is that doped silicon is highly reflective and a fraction of the incident light is lost due to reflectance. Antireflective coatings (ARC), commonly deposited on the surface of solar cells can raise the efficiency of silicon-based PV devices by reducing the light energy lost to reflection. Thus, ARCs offer a means of improving the efficiency not by changing the microelectronics fabrication methods or altering the device chemistry, but by simply adding a thin layer of material onto the top surface of the photovoltaic.

ARCs are often commercially deposited *via* plasma enhanced chemical vapor deposition (PECVD), which offers high coating conformality, high precision and high rates of deposition (*ca.* 20 nm min^{-1}).[8] PECVD films from silicon nitride (SiN) are the industry standard for ARCs on silicon substrates.[8] The disadvantages of using PECVD are the high cost of chemical precursors and of processing in vacuum chambers. The high cost is of particular concern, because the wide use of solar cells as a source of alternative energy is being held back by the high prices of the photovoltaic panels. AR materials deposited by self-assembly have shown promise as an alternative to ARC deposited in a vacuum.[9] Silica and titania sol–gel layers produced *via* spin-coating or dip-coating have been heavily researched and are currently implemented in AR film production.[9–15] The control of the thickness, refractive index and conformality of these films, however, is still a challenge and an area of active research and development. Simple, controllable and scalable deposition, coupled with minimal substrate preparation, is desired from the standpoint of practical applicability in PV devices. Satisfying all these requirements is a challenge for the present self-assembly methods.

Recently, films comprised of layers of nanoparticles have demonstrated potential as an alternative to either sol–gel ARCs or CVD ARCs. They can be composed of a variety of colloidal particulates and deposited by methods such as soft lithographic stamping[16] or layer-by-layer assembly of oppositely charged materials.[17–19] Such techniques can yield effective ARCs but are limited to batch processing and multiple steps. We have reported a technique for controlled convective assembly at high volume fractions that allow single step deposition of porous silica nanocoatings on both glass and silicon substrates.[20] This particle deposition technique takes place at ambient conditions and does not require substrate pretreatment or expensive chemical agents. It is rapid, scalable and well suited for applications that do not require films with a perfect crystalline microstructure. During the process of convective assembly in a thin drying film, the particles are transported from the bulk suspension (at a volume fraction ϕ) to the drying area by a compensating solvent flux as the solvent evaporates. Uniform coatings of several square centimeters could be deposited in tens of minutes from 10–30 μL of colloidal suspensions.[21,22] A species

Department of Chemical and Biomolecular Engineering, North Carolina State University, Raleigh, NC, 27695. E-mail: odvelev@unity.ncsu.edu; Fax: +1 (1)919 513 4365; Tel: +1 (1)919 513 4318
† Presently with the Department of Chemical Engineering, University of California, Santa Barbara, CA 93106.

balance around the drying region allowed us to estimate the thickness of the deposited particle film, h, as

$$h = \frac{K\phi}{v_w(1-\varepsilon)(1-\phi)} \quad (1)$$

where K is a parameter that depends on the relative humidity (or evaporative flux), ϕ is the initial particle volume fraction, $(1 - \varepsilon)$ is the packing fraction of the particles in the film, and v_w is the meniscus withdrawal rate used during the deposition. Our earlier research confirmed the inverse dependence of the film thickness on the meniscus withdrawal rate (or deposition speed), $h \sim 1/v_w$.[20–22] Furthermore, the control over the film thickness permitted fine control over the coating optical properties. For antireflective silica (SiO_2) nanoparticle coatings on glass and silicon, the reduced reflectance of both substrates correlated with the SiO_2 film thickness.[20] The best AR behavior achieved in the earlier work was $\sim$90% reduction in reflectance for glass surfaces and $\sim$50% for smooth single crystal silicon wafer surfaces.

The refractive index of particle films varies with their thickness as the structure and packing fraction varies with the number of layers.[21] We can estimate the refractive index, n_c, of composite coatings made of two or more materials interdispersed in sub-wavelength domains, by a volume average of the species, $n_c = (\phi_p n_p^2 + (1 - \phi_p)n_a^2)^{1/2}$, where ϕ_p is the volume fraction of the particles in the coating, while n_p and n_a are the refractive indexes of the particles and the ambient medium (air in this case), respectively. We found that for films comprised of sub-100 nm silica spheres the reflectance, R, (measured across the ultraviolet to near infrared portion of the spectrum) was well described by a model for a homogeneous uniform thin film (of thickness h and refractive index n_c) on a semi-infinite slab substrate (n_s).[23] Here, R is equal to $|r|^2$, and the Fresnel coefficient of reflection, r, is[20]

$$r = \frac{n_c(n_a - n_s)\cos kh - i(n_s - n_c^2)\sin kh}{n_c(n_a + n_s)\cos kh - i(n_s + n_c^2)\sin kh} \quad (2)$$

where k is the reciprocal space wave number, $k = 2\pi/\lambda n_c$ and λ is the wavelength of light.

All of the particle film deposition techniques mentioned above[15–22] as well as the references in our previous publications[20–22] deal with colloidal particle films on smooth glass, polymer, or silicon surfaces. The nanoparticle coatings in the present study, however, were deposited onto rough polycrystalline solar cells (PCSCs) because of their importance in solar technology. PCSCs are significantly less expensive than their single crystal counterparts, and even though PCSCs have slightly lower photovoltaic efficiencies than single crystal solar cells, they are more cost effective for large scale applications. PCSCs have naturally rough surface microstructure due to the different grain orientations. Understanding the interaction and assembly of particles onto rough surfaces is a complex problem that pertains to a wide variety of different materials and surfaces. Much of the recent work on particle–substrate interactions on rough surfaces has focused on membrane filtration applications.[24] Modelling such interactions is difficult because of the complex geometries involved.[25–27] Both experiments and simulations have found that surface roughness affects membrane adhesion, and more specifically, that particles tend to accumulate in gaps or low regions of the substrate as opposed to taller outward projecting surface features.

In this study, we report the results of convective assembly of ARCs from SiO_2 nanoparticles onto such uneven SC surfaces. The two major goals were to achieve deposition of nanoparticle coatings *via* convective assembly on rough, uneven substrates without chemically modifying either the particles or the substrate surface and to quantify the reduced reflectance and increased electrical output of the photovoltaic cells due to the presence of the silica nanocoatings. Additionally, we investigated the effect of post-deposition silanization of these silica particle films to ascertain whether they could also be made water-repellent.

2 Experimental

2.1 Materials

The nanocoatings were deposited from dispersions of silica nanoparticles of 74 $\pm$ 14 nm in diameter (2.58% by volume) obtained from Polysciences, Inc. (PA). The particles sizes were measured using a Zetasizer (Malvern Instruments, UK). Two types of polycrystalline solar cells were provided from BP Solar (Frederick, MD): uncoated and PECVD SiN-coated. Both types of SCs initially came in square units of 130 cm^2. Each of the units were subsequently broken into smaller portions measuring approximately 5 $\times$ 2.5 cm, taking care to ensure that top and bottom electrode configurations remained intact. The smaller sizes allowed for more convenient deposition and characterization.

2.2 Coating deposition and processing

The convective assembly apparatus used to deposit the coatings is described in detail in our earlier publication.[21] In brief, each coating was made from a $\sim$30 μl drop of silica colloid suspension that was injected into the wedge formed between a glass microscope slide and the solar cell top surface. The droplet was entrapped by capillarity, and the liquid meniscus was withdrawn horizontally across the solar cell surface by translating the upper surface at a controlled rate, v_w, ranging from 5–30 μm s^{-1} (Fig. 1). The moving deposition plate was inclined at an angle of $\sim$23° to the horizontal surface of the solar cell. Coatings were deposited at ambient conditions in the laboratory: 22 $\pm$ 2 °C, and 40–60% RH. In some cases, small amounts of nonionic surfactant ($\sim$0.1% wt.

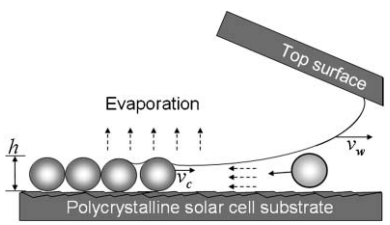

Fig. 1 Schematics of the process of convective deposition of the nanoparticle film on the SC surface (not to scale). The liquid meniscus is being dragged to the right at a constant withdrawal rate v_w, which is equal to the nanocoating deposition speed.

Tween 20, from Aldrich) were used to facilitate wetting of the substrate. For each deposition speed used in the study, a minimum of seven different films were deposited.

After deposition, some films were exposed to silane vapors to test effects of hydrophobizing agents on the coating properties. We used perfluorodecyltrichlorosilane, $F(CF_2)_8(CH_2)_2$-$SiCl_3$, PFDTCS (Oakwook Products, Inc., SC), which forms self assembled close packed monolayers on silica, presenting a 'Teflon-like' outer surface. The substrate was positioned $\approx$1 cm above a small volume of silane placed on the bottom of a Petri dish, and the whole system was closed and kept at ambient conditions. After 15 minutes of exposure at room temperature (previously shown to yield monolayer coverage) the sample was removed, washed gently with ethanol to remove physisorbed PFDTCS molecules, and dried with nitrogen.[28]

2.3 Coating characterization

The reflectance from the coatings of normally incident light was measured using a UV/vis spectrophotometer (Jasco V550, Jasco Corp., Japan) with an integrating sphere attachment over the spectral range of 350–850 nm. All samples were measured at three or more different spots to determine an average sample reflectance.

The microstructure of the coatings was studied with a field-emission scanning electron microscope (JEOL, F6400 operating at 5 kV) using both top-down and cross-sectional secondary electron imaging. In all cases, a sputtered gold–palladium coating of $\sim$50–80 Å was used to improve sample conductivity. For cross-sectional imaging, the samples were fractured in the direction of deposition along the centerline of the coated substrate. Cross-sectional images were obtained using sample mounts with a 60° inclination from the horizontal.

The light source, a Fiberlite 190 fiberoptic lamp (Dolan-Jenner Industries, Inc., MA), was positioned 8 cm above the centerpoint of the solar cell samples. At that distance, the intensity of the light source was mapped as a function of the position relative to the centerline separation (8 cm) using a Laser Q light intensity meter (Coherent, Auburn, CA). The source had a light intensity of $\sim$5.3 mW cm^{-2}. Electrical measurements of the solar cell output current and voltage upon illumination were made with digital multimeters connected to circuits having a range of resistive loads (10 Ω–1 M Ω). Current and voltage readings were taken three separate times at each resistance load and averaged per each sample tested.

The static (sessile drop) contact angle experiments were performed with deionized (DI) water using a Ramé-Hart contact angle goniometer (model 100–00) equipped with a CCD camera, and analyzed with the Ramé-Hart Imaging 2001 software and procedures described in the literature.[28] The contact angles were measured as a function of time after depositing 4–8 μL of the probe liquid on the substrate. The contact angle values reported here are averages of a minimum of 7–10 measurements.

3 Results and discussion

3.1 Microstructure of the polycrystalline silicon solar cells

Three different samples of polycrystalline silicon-based solar cells were studied: uncoated as received, CVD silicon nitride (SiN) coated by the supplier and SiO_2-coated nanoparticle films. The uncoated multicrystalline silicon solar cells had rough microscale topography as revealed by SEM (Fig. 2a,b). These surface roughness features, sometimes microns in

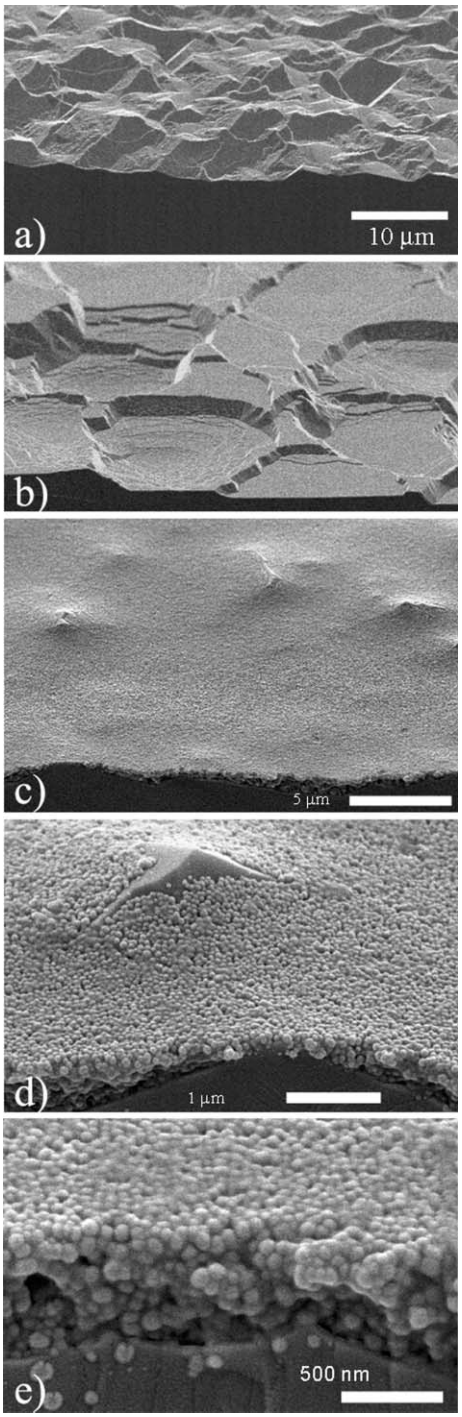

Fig. 2 Microstructure of the SC surface observed by SEM: (a,b) prior to coating, and (c,d,e) after coating with silica nanoparticles at a deposition speed of 6 μm s^{-1}. (a,b) Examples of different surface topographies observed on the bare surface of multicrystalline Si SC (scale = 10 μm). (c) Low magnification cross sectional image of a SiO_2 nanoparticle film deposited on a multicrystalline Si SC substrate (scale = 5 μm). (d,e) Higher magnification images of similar SiO_2 films on silicon SCs (scale for (d) = 1 μm, (e) = 500 nm).

height, were consistently distributed throughout the area of the solar cells. The SiN antireflective coatings deposited by CVD were conformal with the SC surface and could only be distinguished in SEM images by slightly lower atomic number contrast relative to pure silicon, yielding grey films on the top SC surfaces that were about 100 nm thick (not shown).

Lower magnification images of the SiO_2 nanoparticle films showed that the substrates were covered with a uniform coating. Compared to the SiN films on a microscopic level, however, the SiO_2 nanoparticle coatings were not as conformal, nor were they as uniform in thickness. Instead, the SiO_2 particle films exhibited a range of thicknesses across the uneven substrates. In particular, the particles failed to coat regions of the polycrystalline surface having high aspect ratio features such as ridges and edges of the grain boundaries (Fig. 2c–e). The degree of surface coverage decreased with increasing deposition speed. The high aspect ratio features of the silicon substrate became increasingly exposed at faster deposition rates. The fraction of the exposed uncovered surface area (due to high aspect ratio features) estimated by SEM image analysis was on the order of 5% for SiO_2 films deposited in the range of 10–20 μm s^{-1}, which is in reasonably good agreement with the analysis of the reflectance data discussed in the following section. The degree of surface coverage by particle coatings appears to be dependent on the interplay between substrate feature size and particle size. Experiments and simulations using modified DLVO flat plate–particle interactions have shown that depressed regions in rough surfaces are most attractive to particles.[24–27,29] However, it is more likely that the capillary forces in the drying liquid film in our system were guiding the particles into the crevices. Once the high aspect ratio features penetrated through the drying liquid films, capillary forces and evaporation probably packed the assembling particles into the depressed regions of the substrate. Capillary and convective assembly have been used for assembly of particle aggregates into the pits of microfabricated substrates.[30,31]

3.2 Optical properties of the solar cells

The visual appearance and measured reflectance of the three types of solar cells studied are presented in Fig. 3. In all cases, the polycrystalline nature of the silicon substrates was clearly visible by the macroscopic grain boundaries, which yielded local variations in reflectance and color. The uncoated SC exhibited the silvery mirror-like reflectance common for Si covered with a native oxide layer. Macroscopically, the nanoparticle coatings visibly reduced the SC reflectance (Fig. 3a). The profiles of reflectance spectra for the uncoated and SiO_2-coated solar cells were qualitatively similar over the entire spectrum, and hence they appeared similarly colored. However, the SiO_2 ARC decreased the reflectance by $\Delta R \approx 11\%$ (a relative improvement of 30%). The reflected intensity was downshifted across the whole spectrum, resulting in a darker silver coloration for the SiO_2-coated samples. In contrast the SiN-coated substrates were significantly darker in coloration (Fig. 3a). The reflectance of the SiO_2-coated SCs was comparable to the SiN-coated SCs in the near ultraviolet (near UV) and near infrared (NIR) regions of the spectrum. In

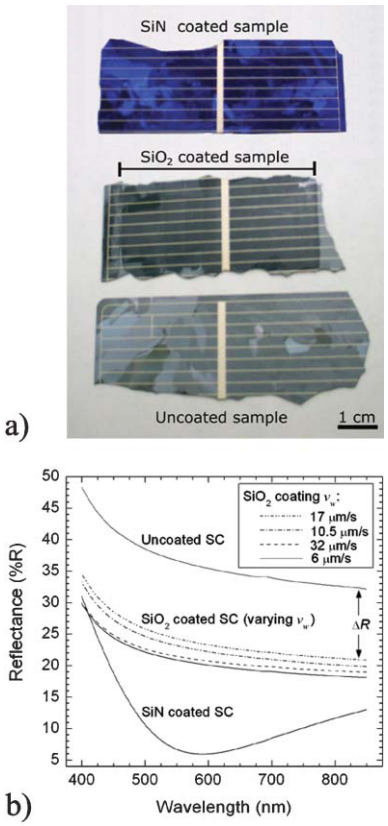

Fig. 3 Optical properties of coated and uncoated multicrystalline silicon solar cells. (a) Visual appearance of PECVD SiN-coated, SiO_2 nanoparticle-coated and uncoated cells. The white lines on the cell surfaces are finger electrodes. (b) Averaged normal incidence reflectance spectra of coated and uncoated SCs. ΔR is the reduction in the SC reflectance provided by the SiO_2 films deposited at different rates.

the visible region, the SiN coating caused a strong reduction in the spectra, approaching ~10% at 600 nm. The bluish coloration typical for the SiN ARC is due to characteristically high reflectance in the blue region of the spectrum relative to longer wavelengths (Fig. 3b).

The reflectance of the SiO_2-coated SCs was dependent on the deposition speed (Fig. 3b), supporting our previous findings for the relation between meniscus withdrawal velocity, layer thickness and AR properties.[20] The thickest SiO_2 coatings deposited at $v_w < 6.3$ μm s^{-1} had the lowest reflectances (Fig. 3b and Fig. 4). At increased deposition speeds, the film thickness and the overall volume fraction of the silica decreased, and correspondingly, the reflectance began to increase. For rates exceeding 25 μm s^{-1}, the reflectance began to decrease again (Fig. 4). The increased reflection at the deposition speed extremes was attributed to scattering from submonolayer voids (for high v_w) or large in-film aggregates (for low v_w).[20]

The reflectance spectra for the uncoated silicon SC could be modelled well using the Fresnel relation, eqn (2) (Fig. 5b). The modelled spectra were calculated assuming a 2 nm thin layer of native oxide layer upon the silicon substrate. The agreement with the experimental measurements proves that grain orientation on the surface has little effect on the optical properties of silicon. Indeed, microscale variations in the spectra are likely

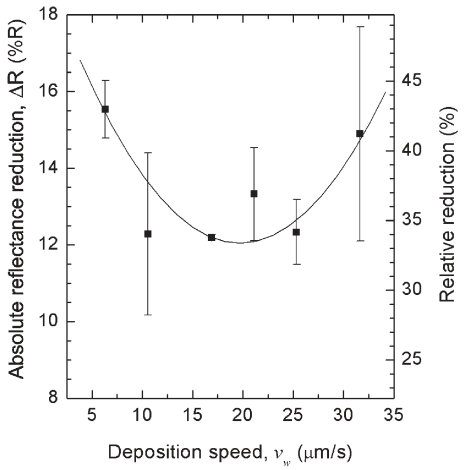

Fig. 4 The reduction in reflectance, ΔR, plotted as a function of deposition velocity, v_w (which controls the silica coating thickness). The data are averaged over the entire range of wavelengths. The relative decrease in the reflectance normalized by one of the uncoated samples is plotted on the right hand axis. The curve is to guide the eye.

averaged out by UV/vis probe beam (of size $\approx$ 5 mm^2). The spectra of factory-deposited SiN ARC were also well fitted using eqn (2) with a single 92 nm layer of SiN (n_c = 1.6), which was in good agreement with the SEM images. The refractive index of SiN, especially in plasma deposited films, can vary depending on the stoichiometric ratios of the feed gases (such as ammonia) used in the CVD process. It typically ranges between 1.7–2.2,[32] so a fit of n_c = 1.6 for the SiN layers on the SCs appears reasonable.

The reflectance spectra of the SiO_2 ARCs could not be modelled by a single homogeneous layer (Fig. 5b). These spectra differ from the previous data for silica nanoparticle films assembled on smooth single crystal silicon wafers, which were well modelled by a homogeneous single layer.[20] Our hypothesis was that the increased variability in the particle film thickness is a result of the rough surface of the multicrystalline SC. The comparatively large beam spot of the UV/vis probe thus averages the optical properties of regions of different film thickness (schematically presented in Fig. 5a). The resulting spectra were thus a weighted combination of the reflectance of all locally different film thicknesses. This hypothesis is in accordance with the microstructural analysis presented in the previous section. Based on the observations with cross-sectional SEM, we modelled the SiO_2 ARC spectra using a distributed film thickness that incorporated five different types of layers: uncovered, monolayer, bilayer, trilayer and tetralayer. The thicknesses and packing fractions of the particles in these layers are listed in Table 1. We assumed that the particles are monodisperse and hexagonally close packed, since the multilayers of square packing are rarely observed and unstable in convectively deposited films.[21] The total area-averaged reflection from the coating was modelled using a distribution of different thicknesses, where each layer of type i has an area-averaged coverage fraction of A_i. Each layer i has a unique thickness, h_i (listed in Table 1). The calculated volume average effective thickness for a given film is $H_{eff} = \Sigma \phi_i h_i$ where the volume fraction of each layer is

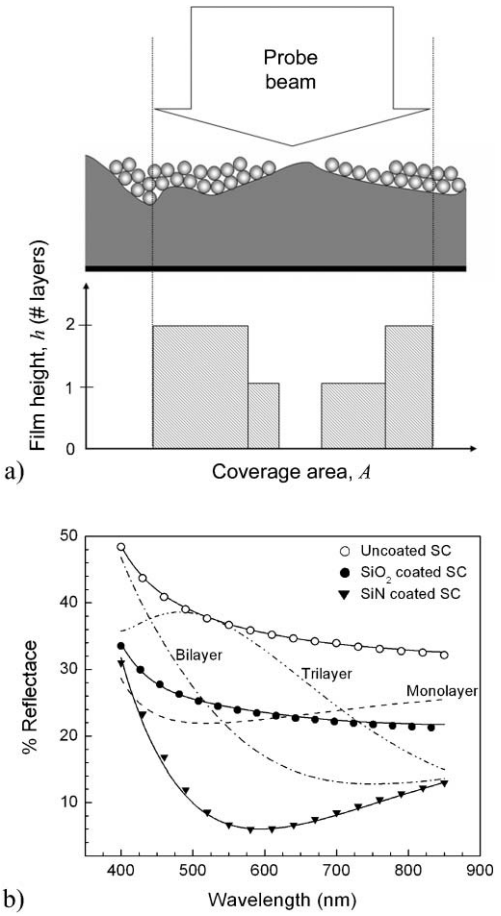

Fig. 5 (a) A schematic illustrating how the spectrometer beam samples regions of multiple thickness and the way in which a weighted thickness can be used to model the reflectance spectra. (b) Reflectance data for the three types of solar cells overlaid with calculated spectra (fitted through eqn (2)). The solid line overlying the data for the uncoated surface was calculated for plain silicon with a 2-nm native oxide layer. The line overlying the SiN-coated sample data was the best fit for a model of a single SiN layer on the Si substrate (l = 92 nm, n_c = 1.6). The line overlying the SiO_2 nanocoating data was fitted by using a model for weighted average thickness or distributed thickness. The dotted and dashed curves illustrate the need for the weighted average model, as no single layer model could accurately fit the SiO_2 film data.

$\phi_i = A_i h_i / \Sigma A_i h_i$. These effective thicknesses provide a set of values, which relate the coating optical properties to the coating microstructure. The reflectance spectra for coatings deposited over a range of deposition speeds were fitted by the least squares method; the thickness distributions obtained are plotted in Fig. 6a.

Table 1 Thickness and packing fraction of films from hexagonally close packed (hcp) particles. The thickness is given in units of particle diameter, D

# Hcp layers	Film thickness (D)	Packing fraction
0	0	0
1	1	0.605
2	1.817	0.666
3	1.663	0.689
4	3.46	0.701

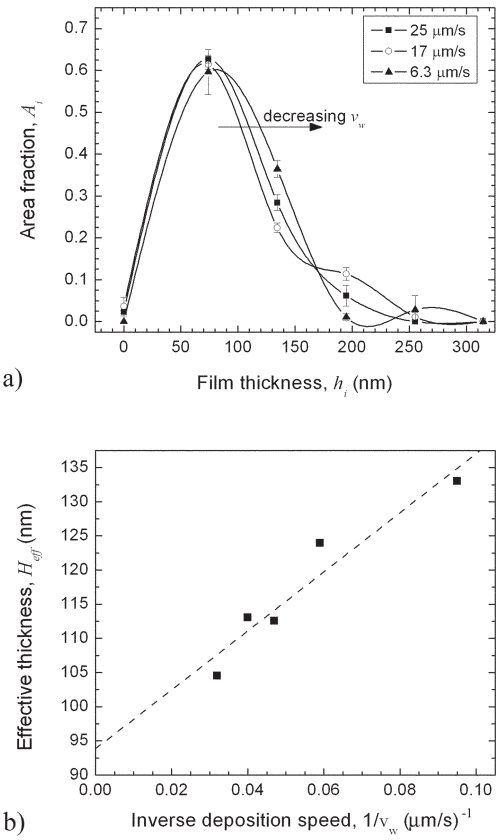

Fig. 6 The fit of the distributed film thickness model indicates that film thickness increases as deposition speed decreases. (a) The area fraction *vs.* film thickness extracted from the best fit of the reflectance data for selected deposition conditions (only three sets of data are shown for clarity). (b) Volume-averaged effective film thickness as a function of inverse deposition speed.

This simple model does not take into account all intricacies of the film structure; however, it describes the spectra effectively. The data show that the effective film thickness increased with decreasing deposition speed, qualitatively following the inverse dependence on deposition speed set by eqn (1) and confirmed in our earlier publications.[20–22] When the values of H_{eff} are plotted against the deposition speed, v_{w}, the trend in the data follows the same inverse linear dependence as the one observed earlier for colloidal coatings on smooth surfaces (Fig. 6b). According to eqn (1), however, the line in Fig. 6b should pass through the origin, *i.e.*, at very rapid meniscus withdrawal speeds the substrate should remain bare. The reason for the non-zero intercept might be that the rough, uneven SC surfaces capture some amounts of particles in the crevices on the material even at very high meniscus withdrawal rates. Qualitatively this is supported by the observation that the 93 nm intercept is close to the size of the individual SiO_2 particles, 74 $\pm$ 14 nm. These H_{eff} values are obtained noninvasively *via* spectroscopy, and do not require the destruction (by fracture) of the sample in order to measure the layer thickness.

3.4 Photovoltaic performance of the coated solar cells

The electrical output of the solar cells was measured by illuminating them with the light source and recording the generated current and voltage (*I–V*) as a function of the resistive load in the circuit. The averaged *I–V* data for uncoated, SiN-coated, and for the optimally performing $\sim$10 μm s^{-1} SiO_2-coated SCs are shown in Fig. 7a. The lowest resistance used was 10 Ω, however, by extrapolation to the zero resistance limit the short-circuit current of these solar cells can be estimated to be $\sim$2 mA cm^{-2} (Fig. 7a). The open circuit voltage, V_{OC}, produced at high resistance was $\sim$450 mV for the SiO_2-coated, $\sim$430 mV for the uncoated SC, and $\sim$350 mV for the SiN-coated SC (see Fig. 7a). The V_{OC} of the coated and uncoated samples compare well with the nominal voltage output of single polycrystalline BP solar cell units ($\sim$0.5 V).

Surprisingly, the *I*, *V* and power outputs of the factory SiN-coated SCs were significantly lower compared to the laboratory SiO_2-coated and even the uncoated SCs. Portions from nearly every solar cell unit in the SiN-coated batch (50 units) were tested, and all yielded similar results. We assume that this is due to a faulty batch of SiN-coated SCs. The goal of this study was to characterize the properties of our SiO_2 ARCs, and the reasons for the poor performance of the factory-made SiN ARCs were not investigated in detail.

The increase in *I–V* output observed in the SiO_2-coated SCs upon illumination was expected and is the main reason why

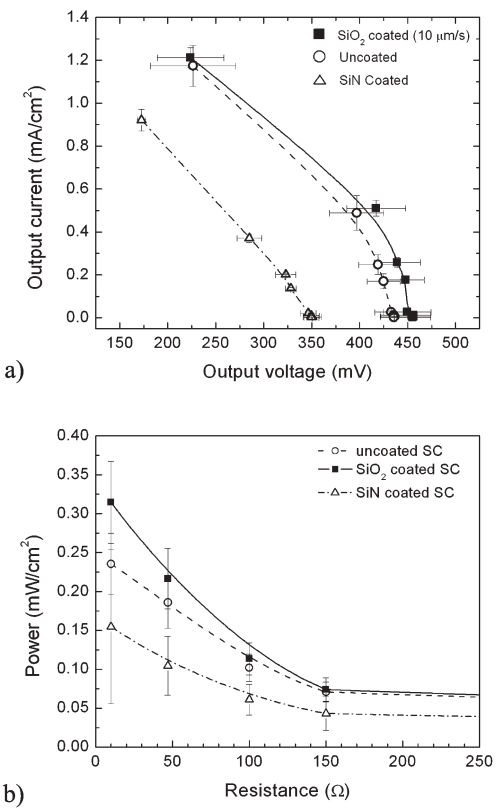

Fig. 7 Photovoltaic power output from illuminated solar cells. (a) Current–voltage (*I–V*) curves for the coated and uncoated SCs. Extrapolation to zero current or zero voltage allowed for estimation of the open circuit voltage ($\sim$450 mV for the coated SC, $\sim$430 mV for uncoated, $\sim$350 mV for the SiN coated) and the short circuit current ($\sim$2 mA cm^{-2} for all cells). (b) Power output of the cells as a function of the resistive load in the circuit. The curves are to guide the eye.

ARCs are used in the photovoltaics industry. In Fig. 7b, the *I–V* data from Fig. 7a was converted to power per solar cell area and replotted as a function of resistive load. The SiO_2-coated samples consistently provided more power at all loads, especially at resistances lower than 150 Ω. At high resistances, the effective power generation became similar for both SiO_2-coated and uncoated SCs eventually becoming zero for open circuit systems. In general these power outputs are low compared to the SC power outputs illuminated by sunlight;[7,33] however, the light source employed for this study was less energetic than solar energy fluxes, which are in the range of 90–130 mW cm^{-2} depending on the time of day, location, and degree of atmospheric absorption.

The relative efficiencies of solar cells coated with SiO_2 nanoparticles deposited at various withdrawal rates were evaluated by measuring the average power output at low circuit resistive loads (averaged over 10 and 50 Ω loads) and plotted in Fig. 8. The benchmark for comparison was the uncoated solar cell power output at low resistance, 0.21 ± 0.03 mW cm^{-2}, represented by the zero line in Fig. 8. These data correlate well with the reflectance reduction data in Fig. 4. The conditions of deposition govern the thickness and effective refractive index of the SiO_2 ARCs,[20] thus playing a crucial role in the ability of the coating to reduce the reflectance, and improve the electrical output of the solar cell. The maximal power output was drawn from coatings deposited between 10 and 25 μm s^{-1}. Very slow deposition speeds ($v_w < 10$ μm s^{-1}) and very rapid deposition speeds ($v_w > 25$ μm s^{-1}) resulted in the least improvement in electrical power generation. It is likely that light power was lost by scattering (hazing) and absorption from the submonolayer voids or from large defects in the thinnest and thickest coatings (experimentally observed in SEM images of such coatings). Regardless of the cause, within experimental error, these thin and thick coatings were no more efficient than uncoated, polycrystalline silicon SCs. Coupled with the results in Fig. 4, the data from Fig. 8 point out the important conclusion that *the lowest reflectance for a coating does not necessarily guarantee maximum power production by the photovoltaic cell*. This might be the reason

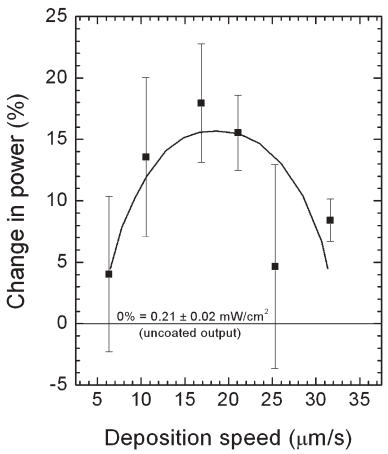

Fig. 8 The relative improvement of the electrical power output of SiO_2-coated SCs as a function of the nanoparticle deposition speed (inversely related to the coating thickness).

Table 2 Summary of the optical properties and electrical power output of the SiO_2, commercial SiN and uncoated SCs. The average reflectance reduction was calculated from a minimum of three samples (calculated on the basis of the difference from the uncoated solar cells across the entire spectrum). The photovoltaic efficiencies were determined by the ratio of irradiation power and electric power output. The irradiation power was ~5.3 mW cm^{-2}

Sample	Reflectance reduction (%*R*)	Power output/ mW cm^{-2}	Efficiency (%)
Uncoated	—	0.21 ± 0.02	4.3 ± 0.4
SiO_2 coated ($v_w \sim 10$ μm s^{-1})	−12.3 ± 2.0%	0.23 ± 0.01	4.7 ± 0.2
SiN coated	−23.9 ± 3.7% –28.9% (at 650 nm)	0.12 ± 0.01	2.5 ± 0.1

why SiN-coated SCs, which were far superior in AR capability, were consistently outperformed in photovoltaic power production.

The measurements reported here illustrate that both the reflectance and the power output per unit area of a solar cell have to be measured and reported in order to evaluate the performance of antireflective coatings. The efficiencies of the SCs compared with the relative improvements in reflectance and power output per unit area are summarized in Table 2. The 11% absolute reduction in the reflectance across the visible spectrum (resulting from SiO_2 coatings) provided a nearly equivalent improvement in the efficiency (~10% relative to the uncoated SC) of the SCs. We also conclude that a completely antireflective coating was not required to boost the power output. Silica nanoparticle ARCs can effectively improve the SC efficiency (Table 2) without prior modification of the surface chemistry of the solar cell and without using vacuum-based coating deposition techniques.

3.5 Post-deposition hydrophobization *via* fluorosilane exposure

The coatings in real solar cell should also have high stability and (ideally) should resist contamination. The porosity of the films from hydrophilic silica nanoparticles may lead to detrimental water uptake and capillary condensation. Other researchers have used this wettability for fabricating super-hydrophilic anti-fogging coatings from films comprised of colloidal silica.[34] Smooth water/silica films result, which do not scatter light from droplets beading on the surface. However, the infused water increases the density of the films, which leads to an increase in the net refractive index of the coatings, and degradation of the antireflectance efficiency. There is, however, a simple way to avoid this issue and add desired functionality to these coatings. The water uptake in porous ceramic films can be reduced by surface modification with chloro- and fluorosilanes.[19,35–38] In fact, periodic surface roughness coupled with particle surface hydrophobicity may make the materials superhydrophobic.[39–45] Such films can be "self-cleaning" as water droplets can bead up and roll off removing dust and debris.[46] Recently, several groups have reported superhydrophobic films made from pre-assembled colloidal crystals, in which the desired microscale surface roughness is provided by the regular bumpiness of the colloidal surface.[47–50]

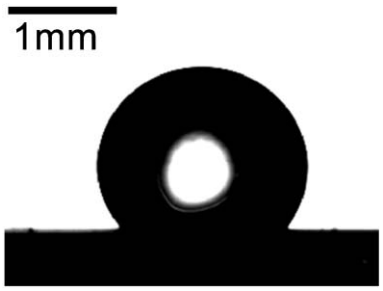

Fig. 9 Micrograph of a static water droplet resting on SiO_2-coated SC surfaces silanized with PFDTCS. The droplet appearance and contact angle of uncoated silanized SC are nearly identical (see Table 3).

We demonstrated that a similar hydrophobization process could be performed to functionalize the colloidal films deposited onto the SC. A self assembled monolayer (SAM) of fluorosilane can prevent moisture and dirt accumulation and make the surface slippery and abrasion-resistant. Potentially, this is also another way to increase device efficiency. Typically, photovoltaics and SCs for outdoor uses are encapsulated in plastic, which provides protection from moisture, dirt and abrasion. However, this plastic encasement reduces further the device efficiency due to the reflectance loss from the outer surface of the plastic film. The fluorosilane SAM alternative coating has a low refractive index ($\sim$1.35) and a thickness of approximately one molecular length ($\sim$10–20 Å), so that its contribution to the reflectance is minimal.

The experiments were performed with SCs coated at v_w = 10 μm s^{-1} and uncoated control SCs, which were exposed to silane vapors. There was no discernible difference in the optical properties or power output of the coated or uncoated SCs after silanization with PFDTCS. Prior to silane exposure, the surfaces of both samples were fully wettable (near vanishing contact angle), due to the presence of the native oxide layer on the SC surface in the control case, and due to the porous SiO_2 particle layer in the coated case. The effect of the hydrophobization process on the wettability of the substrates is illustrated in Fig. 9. After exposure to the PFDTCS, for both the SiO_2 ARC and the uncoated control SC substrate, the water no longer penetrated into the surface and the measured static contact angle increased to $\sim$120° (Fig. 9). The contact angles measured before and after treatment are listed in Table 3.

Interestingly, both the uncoated control surfaces and the silica coatings covered with PFDTCS had the same contact angle, within the experimental error. Our initial hypothesis was that the roughness of the silica films would enhance the hydrophobicity of the fluorosilane layer (since others have shown that regular microscale roughness can lead to superhydrophobic surfaces).[47–50] However, it appears that the roughness and porosity of the ARC coatings comprised of $\sim$70 nm particles were on too small a scale for effectively imparting surface superhydrophobicity. Balancing the optical and superhydrophobic properties of such surfaces might be a challenge, since the addition of larger particles to make these films rougher may improve the post-deposition hydrophobicity, but might also negatively impact the antireflective capabilities through larger scattering losses. Nevertheless, the results prove that post-deposition hydrophobization is effective in solving the problem of water uptake and could improve the coatings in a variety of ways. Alkylsilanes or dialkylsilanes might, however, be preferred to fluorosilanes in industrial implementation of such techniques due to their lower cost.

Table 3 The average contact angles onto the SCs measured before and after silanization with PFDTCS

Sample	θ_c before silanization	θ_c after silanization
Uncoated	$< 20°$	$124 \pm 7°$
SiO_2 coated	$< 20°$	$119 \pm 7°$

4 Concluding remarks

Convective assembly was successfully used to deposit silica nanoparticle coatings on multicrystalline silicon surfaces, even though the roughness of these substrates was significantly greater than the flat surfaces that are typically studied. These nanocoatings improved the performance of the photovoltaic cells. While these silica nanoparticle coatings do not provide the photovoltaic efficiencies seen in PECVD SiN or SiO_2 ARCs ($\sim$15%),[33] they are on a par with or better than the $\sim$5% efficiencies of other alternative nanoparticulate SC systems.[5,7,51] Potentially, nanoparticles smaller than 50 nm in diameter can be used to obtain more conformal coatings on multicrystalline SCs. The nanoparticle ARCs for SCs can be further optimized by employing different metal oxides (*e.g.*, ZrO_2 or TiO_2) to better tune the refractive index of the coatings. The results also lead to the methodological conclusion that the true test of ARC performance is the power increase, not the reduction in reflectance. The properties of these coatings can be improved by post-deposition functionalization of the surfaces of the silicon nanoparticles with perfluorosilane SAMs. The surfaces of such nanoparticle films can eventually be made to be water-repellent and self-cleaning. The scalability and low cost of the techniques allow for practical application in mass produced solar cells and other technologies.

Acknowledgements

This work was funded in part by STC Program of the National Science Foundation under Agreement No. CHE-9876674, an NSF CAREER Award, and the NC State University Alliances for Graduate Education and the Professoriate (AGEP). We thank Jay Miller and BP Solar (North America) for providing samples of SiN-coated and uncoated solar cells. We also thank Greg Parsons for the use of a light meter, Dale Bachelor for assistance with the SEM, and Julie Crowe and Kirill Effimenko for assistance with the silanization and contact angle measurements.

References

1 M. K. Nazeeruddin, A. Kay, I. Rodicio, R. Humphrybaker, E. Muller, P. Liska, N. Vlachopoulos and M. Gratzel, *J. Am. Chem. Soc.*, 1993, **115**, 6382–6390.
2 T. Buonassisi, A. A. Istratov, M. A. Marcus, B. Lai, Z. H. Cai, S. M. Heald and E. R. Weber, *Nat. Mater.*, 2005, **4**, 676–679.
3 IEA-PVPS Newsletter, *PV Power*, 2001, **14**, 1–8.

4 A. Shah, P. Torres, R. Tscharner, N. Wyrsch and H. Keppner, *Science*, 1999, **285**, 692–698.
5 N. Camaioni, G. Ridolfi, V. Fattori, F. Favaretto and G. Barbarella, *J. Mater. Chem.*, 2005, **15**, 2220–2225.
6 R. Ebner, M. Radike, V. Schlosser and J. Summhammer, *Prog. Photovoltaics*, 2003, **11**, 1–13.
7 G. K. Kiema, M. J. Colgan and M. J. Brett, *Sol. Energy Mater. Sol. Cells*, 2005, **85**, 321–331.
8 P. Doshi, G. E. Jellison and A. Rohatgi, *Appl. Opt.*, 1997, **36**, 7826–7837.
9 D. G. Chen, *Sol. Energy Mater. Sol. Cells*, 2001, **68**, 313–336.
10 D. R. Uhlmann, T. Suratwala, K. Davidson, J. M. Boulton and G. Teowee, *J. Non-Cryst. Solids*, 1997, **218**, 113–122.
11 A. Gombert, W. Glaubitt, K. Rose, J. Dreibholz, C. Zanke, B. Blasi, A. Heinzel, W. Horbelt, D. Sporn, W. Doll, V. Wittwer and J. Luther, *Sol. Energy*, 1998, **62**, 177–188.
12 P. Nostell, A. Roos and B. Karlsson, *Thin Solid Films*, 1999, **351**, 170–175.
13 Q. Y. Zhang, J. Wang, G. Wu, J. Shen and S. Buddhudu, *Mater. Chem. Phys.*, 2001, **72**, 56–59.
14 P. K. Biswas, P. S. Devi, P. K. Chakraborty, A. Chatterjee, D. Ganguli, M. P. Kamath and A. S. Joshi, *J. Mater. Sci. Lett.*, 2003, **22**, 181–183.
15 O. Harizanov and A. Harizanova, *Sol. Energy Mater. Sol. Cells*, 2000, **63**, 185–195.
16 H. Y. Koo, D. K. Yi, S. J. Yoo and D. Y. Kim, *Adv. Mater.*, 2004, **16**, 274–277.
17 J. Hiller, J. D. Mendelsohn and M. F. Rubner, *Nat. Mater.*, 2002, **1**, 59–63.
18 H. Hattori, *Adv. Mater.*, 2001, **13**, 51–54.
19 J. H. Rouse and G. S. Ferguson, *J. Am. Chem. Soc.*, 2003, **125**, 15529–15536.
20 B. G. Prevo, Y. Hwang and O. D. Velev, *Chem. Mater.*, 2005, **17**, 3642–3651.
21 B. G. Prevo and O. D. Velev, *Langmuir*, 2004, **20**, 2099–2107.
22 B. G. Prevo, J. C. Fuller and O. D. Velev, *Chem. Mater.*, 2005, **17**, 28–35.
23 G. R. Fowles, *Introduction to Modern Optics*, Dover Publications, Inc., 1989.
24 E. M. V. Hoek, S. Bhattacharjee and M. Elimelech, *Langmuir*, 2003, **19**, 4836–4847.
25 S. Bhattacharjee, C. H. Ko and M. Elimelech, *Langmuir*, 1998, **14**, 3365–3375.
26 L. Suresh and J. Y. Walz, *J. Colloid Interface Sci.*, 1997, **196**, 177–190.
27 J. Y. Walz, *Adv. Colloid Interface Sci.*, 1998, **74**, 119–168.
28 J. Genzer, K. Efimenko and D. A. Fischer, *Langmuir*, 2002, **18**, 9307–9311.
29 J. Nalaskowski, S. Veeramasuneni, J. Hupka and J. D. Miller, *J. Adhes. Sci. Technol.*, 1999, **13**, 1519–1533.
30 K. P. Velikov, C. G. Christova, R. P. A. Dullens and A. van Blaaderen, *Science*, 2002, **296**, 106–109.
31 Y. N. Xia, Y. D. Yin, Y. Lu and J. McLellan, *Adv. Funct. Mater.*, 2003, **13**, 907–918.
32 *TimeDomain CVD, Silicon Nitride: Properties and Applications*, http://timedomaincvd.com/CVD_Fundamentals/films/SiN_properties.html.
33 H. E. Elgamel, A. M. Barnett, A. Rohatgi, Z. Chen, C. Vinckier, J. Nijs and R. Mertens, *J. Appl. Phys.*, 1995, **78**, 3457–3461.
34 F. C. Cebeci, Z. Z. Wu, L. Zhai, R. E. Cohen and M. F. Rubner, *Langmuir*, 2006, **22**, 2856–2862.
35 J. I. Jung, J. Y. Bae and B. S. Bae, *J. Mater. Chem.*, 2004, **14**, 1988–1994.
36 C. M. Yang, A. T. Cho, F. M. Pan, T. G. Tsai and K. J. Chao, *Adv. Mater.*, 2001, **13**, 1099–1102.
37 R. M. de Vos, W. F. Maier and H. Verweij, *J. Membr. Sci.*, 1999, **158**, 277–288.
38 K. Y. Huang, Z. P. He and K. J. Chao, *Thin Solid Films*, 2006, **495**, 197–204.
39 H. J. Busscher, I. Stokroos, H. C. Vandermei, P. G. Rouxhet and J. M. Schakenraad, *J. Adhes. Sci. Technol.*, 1992, **6**, 347–356.
40 T. Onda, S. Shibuichi, N. Satoh and K. Tsujii, *Langmuir*, 1996, **12**, 2125–2127.
41 J. Bico, C. Marzolin and D. Quere, *Europhys. Lett.*, 1999, **47**, 220–226.
42 A. Nakajima, A. Fujishima, K. Hashimoto and T. Watanabe, *Adv. Mater.*, 1999, **11**, 1365–1368.
43 M. Miwa, A. Nakajima, A. Fujishima, K. Hashimoto and T. Watanabe, *Langmuir*, 2000, **16**, 5754–5760.
44 A. Nakajima, K. Hashimoto, T. Watanabe, K. Takai, G. Yamauchi and A. Fujishima, *Langmuir*, 2000, **16**, 7044–7047.
45 Z. Yoshimitsu, A. Nakajima, T. Watanabe and K. Hashimoto, *Langmuir*, 2002, **18**, 5818–5822.
46 R. Blossey, *Nat. Mater.*, 2003, **2**, 301–306.
47 G. Zhang, D. Y. Wang, Z. Z. Gu and H. Mohwald, *Langmuir*, 2005, **21**, 9143–9148.
48 E. Hosono, S. Fujihara, I. Honma and H. S. Zhou, *J. Am. Chem. Soc.*, 2005, **127**, 13458–13459.
49 G. Gu, H. Dang, Z. Zhang and Z. Wu, *Appl. Phys. A*, 2006, **83**, 131–132.
50 J. Li, J. Fu, Y. Cong, Y. Wu, L. J. Xue and Y. C. Han, *Appl. Surf. Sci.*, 2006, **252**, 2229–2234.
51 J. B. Baxter and E. S. Aydil, *Appl. Phys. Lett.*, 2005, **86**, 053114.